Optical Scattering by Dense Disordered Metal Nanoparticle Arrays

Juris Prikulis, Uldis Malinovskis, Raimonds Poplausks, Indra Apsite, Gatis Bergs & Donats Erts

Volume 8 · Number 4 · Dec

plasmonics

ONLINE FIRST

Springer

11468 · ISSN 1557-1955
8(4) 1515–1712 (2013)

Springer

Springer

Optical Scattering by Dense Disordered Metal Nanoparticle Arrays

**Juris Prikulis · Uldis Malinovskis ·
Raimonds Poplausks · Indra Apsite · Gatis Bergs ·
Donats Erts**

Abstract We address the optical properties of dense disordered yet well-separated metal nanoparticle arrays produced by physical vapor deposition through anodized aluminum oxide membrane masks. Using variations in synthesis parameters, the particle diameters vary from 14 to 50 nm and average center separation from 45 to 112 nm. Ag nanoparticle arrays with no long-range periodicity exhibit apparently random formation of high-intensity depolarized regions relative to orientation of incident electric field. We analyze this behavior numerically using coupled dipole model and explain the contrast formation in recorded scattering images.

Keywords Plasmon resonance · Silver · Nanoparticle arrays · Ultrathin anodized aluminum oxide membrane · Depolarization

Introduction

Metallic nanostructures are interesting for numerous reasons including practical applications in catalysis [1], biosensors [2], surface-enhanced Raman spectroscopy (SERS) [3], solar cells [4], photodetectors [5], waveguides [6], and color filters [7] or are used as model systems for theoretical studies of various physical phenomena [8, 9]. Much of attention has been directed towards regular nanoparticle arrays [10–12], because certain properties can be greatly enhanced or suppressed due to grating coupling effects. In addition,

J. Prikulis (✉) · U. Malinovskis · R. Poplausks · I. Apsite ·
G. Bergs · D. Erts
Institute of Chemical Physics, University of Latvia, Riga, Latvia
e-mail: juris.prikulis@lu.lv

periodicity simplifies calculations, since all elements in an infinitely repeating system are equivalent and the influence from surrounding at each site is the same. In this case, elegant semianalytical expressions can be found for description of recorded spectra [13].

Well-defined nanostructure arrays for plasmonics studies are often produced using electron beam lithography [12, 14, 15]. Alternative recipes for nanoparticle array production include colloid deposition [7, 16], colloidal lithography [17], nanosphere lithography [18], scanning probe lithography [19], or nanoimprint technology [20]. Particle diameter of 14–50 nm, and center-to-center separation of 45–112 nm, which is of interest in this study, is on the boundary between size ranges where mentioned top-down or bottom-up synthesis reaches their limits. We therefore employ the self-assembly process of pores in anodized aluminum oxide (AAO) to produce masks for nanoparticle array deposition using a modification of the original method by Masuda and Satoh [21]. Nanoparticle arrays of this type have previously been used, e.g., as SERS substrate [22] or proposed for enhancement of solar cells [23]. The pores can be grown to a well-ordered regular hexagonal structure [24]; however, thin AAO layers suitable for masked deposition and consequently the produced nanoparticle arrays tend to be disordered. Such systems are much less studied in comparison to regular arrays or individual nanoparticles.

In this work, we address the optical properties of disordered arrays, where periodicity-based simplification is no longer valid and the interaction between nanoparticles results in a new metamaterial with distinct features in a scattered field. In particular, we observe a polarization-dependent grain structure in microscopy images, where recorded interference patterns are highly sensitive to exact experimental conditions and are radically different at array boundaries. Using a coupled dipole model, where each

nanoparticle is represented by an ellipsoid polarizability, we obtain scattering spectra and simulated microscopy images, which are consistent with experimental observations.

The set of parameters which define the scope of this work is as follows: Firstly, the particle sizes on a glass substrate are much smaller and more dense than what has been reported on similar disordered (short range ordered) assemblies [17, 25]. Typically, particle diameters exceed 50 nm and separation is larger than 100 nm also including studies of periodic systems. Consequently, in our case, a strong near-field interparticle coupling can be expected, and the resulting optical response cannot be treated as a simple sum of individual scatterers. Secondly, although in their nearest surrounding the particle separation is nearly constant, the system lacks periodicity at distances exceeding the wavelength of incident visible light. This is opposite to arrays studied in ref. [14, 15], where disorder introduced by random displacement of nanoparticles from their regular grid pattern preserves the long-range periodicity. Thirdly, the particles are densely packed, yet well separated, in contrast to less uniformly distributed arrays obtained by colloid deposition, where individual grains may form connected aggregates even at moderate array densities.

Experiment

For brevity, we only summarize the steps of sample preparation, which is described in detail in ref. [26]. AAO membranes were synthesized in a two-stage anodization process on a high-purity aluminum foil. The pore separation and degree of order can be varied by choice of electrolytic solution and anodization voltages [24]. For the samples shown in panels a and b and panels c and d in Fig. 1, 0.3 M

sulfuric and 0.3 M oxalic acids, respectively, were used. In an earlier work by our group [26], it was shown that exceptionally thin (64 nm) AAO membranes with pore diameters below 20 nm can be produced. In the next stage, the AAO membrane was coated with poly(methyl methacrylate) PMMA and covered by a thick layer of paraffin which serves as a transport substrate. Thereafter, aluminum foil was dissolved by a mixture of $CuCl_2$ and HCl, followed by barrier layer removal in 10 wt% H_3PO_4. The obtained dry membrane was then placed on a plasma-cleaned standard microscope cover glass. PMMA together with paraffin was removed by a flow of oxygen gas at elevated temperature. Thin Cr layer for improved adhesion and Ag layer of selected thickness were sputtered using an etching and coating system (Gatan 682) through the AAO membrane. Finally, after removal of AAO either using an adhesive tape or etching with 1 M NaOH solution, Ag nanoparticle arrays on glass were ready. The resulting particle size and array structure were analyzed using the scanning electron microscope (SEM) Hitachi S-4800. Using the same method, we have produced similar arrays of other material nanoparticles including Au, which also is of interest in plasmonic applications.

For measurement of optical scattering, we used a dark-field configuration of an Olympus IX71 microscope with a U-TLD condenser lens (numerical aperture NA= 0.9) and glass-compensated objective lens LUCPlanFLN 60X (NA= 0.7). The spectra were recorded using the spectrometer Ocean Optics USB4000 connected to the microscope using an optical fiber with a core diameter of 50 μm and images captured using the digital camera Nikon D100.

Three distinct surface coverage patterns can be found on each sample, namely, regions with residues of AAO membrane coated by metal film, nanoparticle arrays, and

Fig. 1 Scanning electron microscope images of Ag nanoparticle arrays. The sample labeling **a**–**d** is maintained throughout this paper and parameters are listed in Table 1
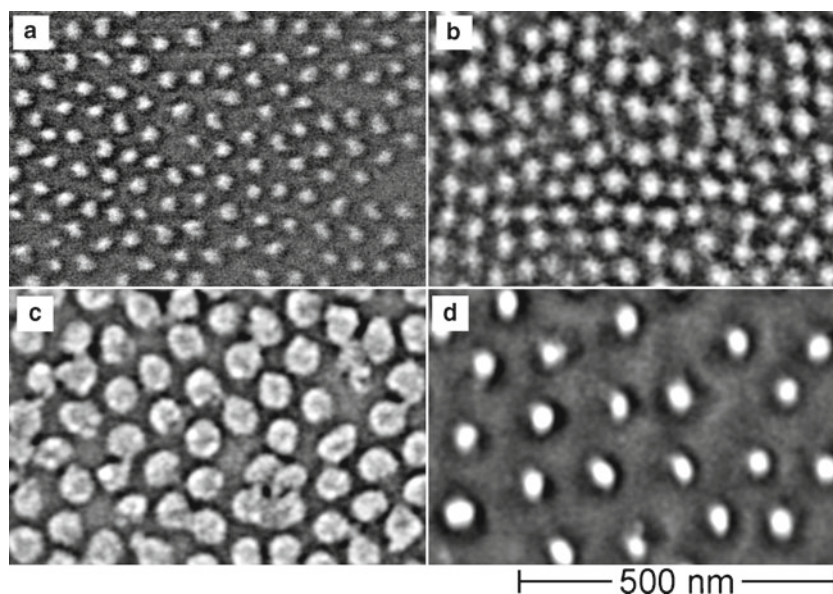
empty zones, where no pores have been formed during mask production due to irregularities in aluminum foil. These patterns are identified by inspection in SEM and can be clearly distinguished using bright-field and dark-field optical microscopes. In SEM observation, typical arrays have uniform size distribution with regions of varying density (missing particles due to incomplete barrier layer removal), which appear as smooth variations of brightness and color in optical images. Spectral measurements are done on uniform array regions, farthest from metal film edges, which are much brighter than the arrays and array boundaries to empty zones, and would distort the spectra or saturate the image detector.

Numerical Method

Due to their small size, each particle can be treated as a dipole scatterer reacting to the incident radiation and the sum of dipole fields produced by all other particles. Particle coordinates x_j and y_j are randomly generated in $z = 0$ plane in a sequence, where each next particle position is accepted only if its distance to every previously stored particle is greater than a certain threshold. The resulting array is thereafter scaled so that its maximum position σ of radial distribution function (RDF) $g(r)$ matches the measured value for corresponding sample (Table 1). Finally, $N = 2,000$ particles within a circular area are selected for calculations (Fig. 2a). Depending on density, this amount of nanoparticles occupies approximately a 10-μm^2 surface area $S_{2,000}$ (Table 1), which can be analyzed in detail using an optical microscope. Calculations on this number of particles can be easily managed using a desktop computer and are also sufficient to capture the properties of systems under investigation as will be discussed later.

In order to find all induced dipole moments, we follow the problem formulation by Draine and Flatau [27] with adjustments to capture the fact that the dipoles are noncontiguous ellipsoids and do not reside on a regular lattice. This approach is known as coupled dipole (CD) approximation and has been used to model optical properties of nanoparticle pairs [28], linear nanoparticle chains, and two-dimensional arrays with various structures [13, 14].

Table 1 Summary of nanoparticle array sample parameters

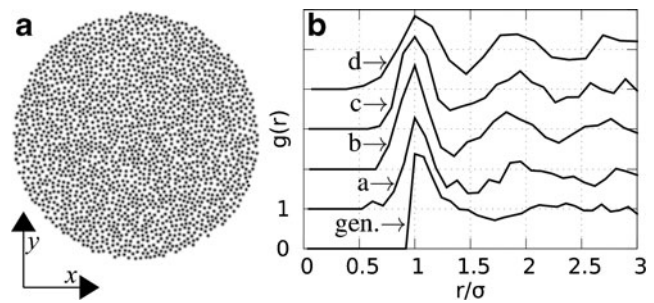| Sample	a	b	c	d
Separation σ, nm	45	51	68	112
Diameter, nm	14	22	50	26
Diameter std. dev.	12 %	10 %	7 %	10 %
Height, nm	6	6	14	10
Area $S_{2,000}$, μm^2	5.81	7.47	13.3	36.0

Fig. 2 **a** Generated nanoparticle array with $N = 2,000$ elements. **b** Radial distribution function (RDF) of particles shown in Fig. 1 and generated array. Each RDF is shown with integer offset for clarity, and maximum position σ for corresponding sample is listed in Table 1

We assume that all nanoparticles are identical spheroids with principal axis oriented along the Cartesian coordinate system. Their polarizability volume tensor α is diagonal and we use empirical expressions from ref. [29] which are in good agreement with experimental observations on individual nanoparticles with dimensions similar to those used in current study. Following this method, the value of α along each axis is calculated using

$$\alpha = \frac{V}{\left(L + \frac{\varepsilon_m}{\varepsilon - \varepsilon_m}\right) + A\varepsilon_m\chi^2 + B\varepsilon_m^2\chi^4 - i\frac{\pi^2\varepsilon_m^{3/2}}{3}\frac{V}{\lambda_0^3}}, \quad (1)$$

where V is the particle volume, $\varepsilon_m = 1.75$ is the effective dielectric constant for the glass–air interface, and L is the shape factor [30], while $A(L)$ and $B(L)$ are empirically determined coefficients [29]. Here, $\chi = k_0 a$ is dimensionless size parameter, a is the length of the corresponding spheroid semiaxis, $k_o = 2\pi/\lambda_0$ is the vacuum wave number, and λ_0 is the vacuum wavelength of the incident radiation. For the dielectric function ε, we use values for silver from ref. [31]. It should be noted that other models for estimation of α and ε_m could be used to describe nanoparticles on glass–air interface as was done, e.g., in refs. [17, 28]; moreover, ε_m is sometimes used as a fitting parameter [32].

In the next step, we construct the set of linear equations

$$\sum_{k=1}^{N} \mathsf{A}_{jk}\mathbf{P}_k = \mathbf{E}_{\text{inc},j}, \quad (2)$$

where A_{jk} is a 3×3 matrix.

$$\mathsf{A}_{jk} = \frac{\exp(ikr_{jk})}{r_{jk}}$$
$$\times \left[k^2(\hat{r}_{jk}\hat{r}_{jk} - 1_3) + \frac{ikr_{jk} - 1}{r_{jk}^2}(3\hat{r}_{jk}\hat{r}_{jk} - 1_3) \right] \quad (3)$$

for $j \neq k$ and

$$\mathsf{A}_{jj} = 4\pi\alpha_j^{-1} \quad (4)$$

In these equations, $\mathbf{P}_k$ are dipole moments of each particle to be found and $\mathbf{E}_{\mathrm{inc},j} = \mathbf{E}_0 \exp(i\mathbf{k} \cdot \mathbf{r}_j)$ is the incident electric field at particle j. Orientation of $\mathbf{E}_0$ and wave vector in medium $\mathbf{k}$ are used to control the polarization, angle of incidence θ, and azimuth ϕ. Further, $r_{jk} = |\mathbf{r}_j - \mathbf{r}_k|$, $\hat{r}_{jk} = (\mathbf{r}_j - \mathbf{r}_k)/r_{jk}$, and 1_3 is a 3×3 identity matrix. Note that the factor 4π in Eq. 4 is included in the definition of polarizability α in ref. [27].

The matrix A, which is built from $N \times N$ blocks of A_{jk}, is complex and symmetric and we use the corresponding LAPACK routine [33] for solving the set of equations with multiple right-hand sides. The benefit of this approach is that the values of $\mathbf{P}_j$ at given wavelength can be obtained for a set of angles θ, ϕ and polarizations in a single run.

Finally, the scattering cross section is obtained by numerical integration of the far-field radiated power by induced dipole moments [34].

$$C_{\mathrm{sca}} = \frac{k^4}{|\mathbf{E}_0|^2} \int d\Omega \left| \sum_j \left[\mathbf{P}_j - \hat{\mathbf{n}}(\hat{\mathbf{n}} \cdot \mathbf{P}_j) \exp(-ik\hat{\mathbf{n}} \cdot \mathbf{r}_j) \right] \right|^2 , \tag{5}$$

where $\hat{\mathbf{n}}$ is a unit vector in the direction of scattering and $d\Omega$ is an element of solid angle.

For understanding the image formation in the dark-field (DF) microscope, we assume that each particle acts as a point source with strength proportional to the induced dipole moment $\mathbf{P}_j$, which is a complex vector. Each particle produces an Airy pattern or point spread function of an ideal lens [35], which coherently add to produce the image

$$I_{(\mathrm{r,g,b})}(x, y) = \left| \sum_j \frac{P_{j(x,y,z)} J_1(v_j)}{v_j} \right|^2 , \tag{6}$$

where J_1 is the Bessel function of the first kind and v_j is a dimensionless lateral coordinate

$$v_j(x, y) = \sqrt{(x - x_j)^2 + (y - y_j)^2} \frac{2\pi}{\lambda} \mathrm{NA}. \tag{7}$$

Here, NA is the numerical aperture of the objective lens. The images are constructed for each wavelength with pseudo-colors, where red, green, and blue channels represent intensity $I_{(\mathrm{r,g,b})}$ computed for $\mathbf{P}_j$ components parallel to the (x,y,z) axis of the coordinate system.

Results and Discussion

The scattering spectra and DF images (Fig. 3) were recorded using natural (unpolarized) illumination. The scattering maximum is clearly in the blue-green region; however, we notice that firstly, the array boundaries to areas with missing particles are more intense and of somewhat different color, most clearly pronounced for sample (a), and secondly, there is a granular structure inside the uniform array with notable color variations, most visible for sample (c).

For simulations at each wavelength, it was assumed that the sample is illuminated by a plane wave, either S- or

Fig. 3 Measured scattering spectra (blue dots) of samples a–d in Fig. 1. Calculated scattering cross sections of entire array (N particles) for illumination with S-polarized (red line) or P-polarized (green line) light. Insets show DF photographs of approximately 50×50-$\mu\mathrm{m}^2$-large area
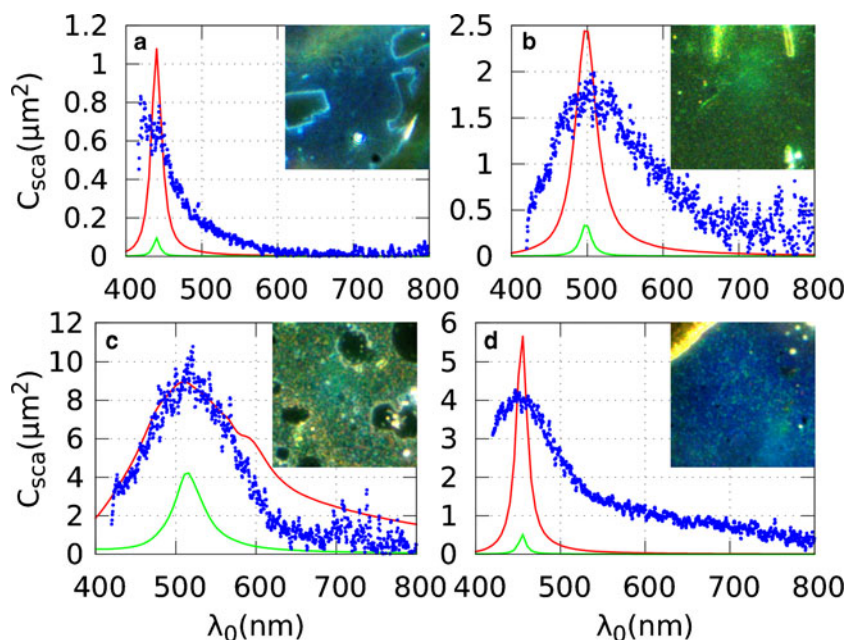
Fig. 4 a–h Simulated DF images with coherent illumination. In the *upper row*, the *red channel* (I_x) was amplified 23 times; in the second row, the *green* channel (I_y) was amplified 10 times. **i** Nanoparticle array with natural DF illumination, **j** the same sample illuminated using 488-nm S-polarized laser source and parallel arrangement of polarization filter in imaging path, and **k** the same with perpendicular polarization filter arrangement
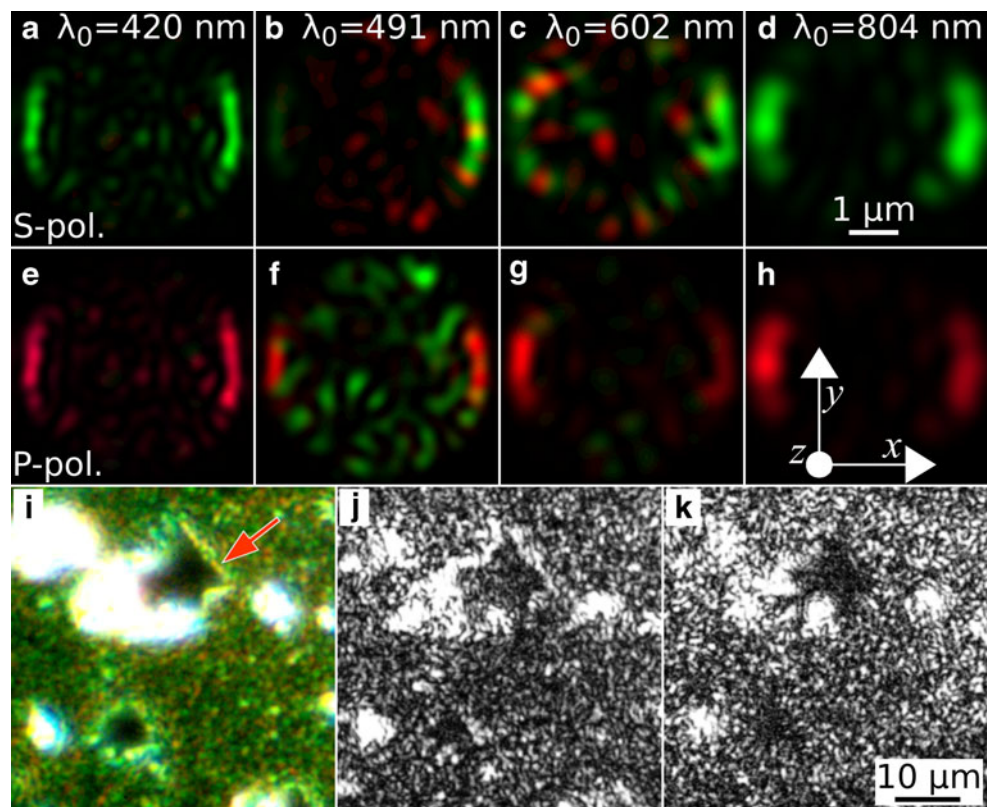
P-polarized, with angle of incidence $\theta = 65°$, which corresponds to the numerical aperture of the condenser lens. For samples (a), (b), and (d), the simulations underestimate the width of the spectral peak, while for sample (c), the calculated spectra are somewhat broader.

There are several factors which may explain the differences between widths of calculated and measured spectra, namely, the model does not include particle size and shape distribution, while diameter standard deviation obtained from SEM images is $\approx 10\,\%$ (Table 1), and the calculated spectra integrate the electric fields from the whole array over entire closed sphere, whereas measurements are done on a small fraction of the array in a limited solid angle. The particle height was estimated from fitting the maximum of calculated spectra to experimental observations and agrees

within $\approx 50\,\%$ of target parameters of the sputtering process. The uncertainty arises from uneven coating thickness and portions of sputtered material covering AAO membrane walls and obstructing the path to the glass surface. Unfortunately, it was too difficult to locate the corresponding area of the sample using AFM, which would provide more accurate measurement of nanoparticle height. A further difference between the simulated arrays and actual samples is that the latter is somewhat more ordered as can be observed in RDF (Fig. 2b). One could increase the order in simulated arrays by allowing the coordinates to relax in, e.g., 6–12 potentials; however, such study is beyond the scope of this article. Nevertheless, we note the tendency of spectral broadening which is consistent with experimental observations. The width of the resonance peak is largest in cases

Fig. 5 Calculated depolarization ratios for samples **a**–**d** listed in Table 1 illuminated at $\theta = 65°$ incidence and different polarizations
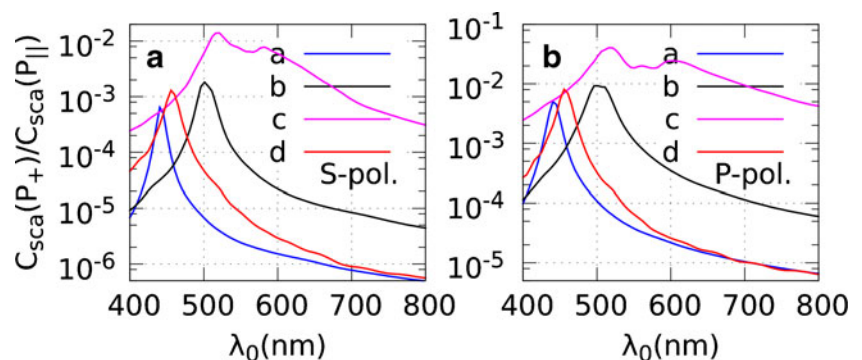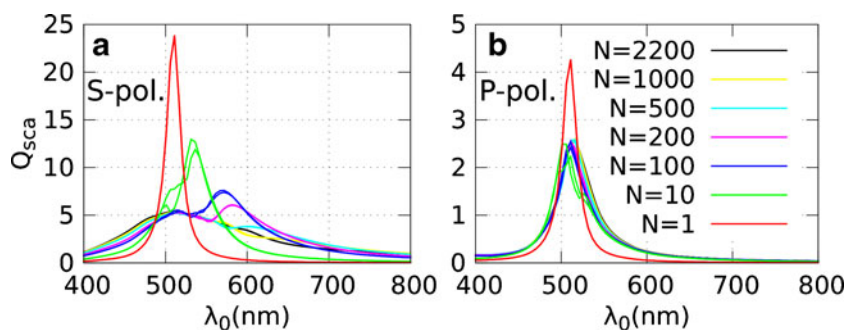
Fig. 6 Calculated scattering efficiency spectra for arrays of various sizes illuminated at $\theta = 65°$ incidence

when gaps between the particles are smallest relative to their size.

The important observation is a considerable depolarization of scattered light in simulated and captured images. Namely, S-polarized incident radiation with electric field parallel to the y axis (Fig. 4a–d) produces portions of an x-oriented scattered field, and similarly, P-polarized radiation with electric field in the x,z plane (Fig. 4e–h) is partially scattered with electric field along the y axis. The intensity of scattered light parallel to incident electric field always appears highest at array edges, while depolarized grain structure within the array is visible only at wavelengths near the scattering maximum. Such behavior can also be observed experimentally.

A sample similar to case (c) was illuminated by a 488-nm S-polarized laser beam at angle of incidence $\theta = 65°$. Figure 4j was taken with a polarization filter orientation, which maximizes the image brightness (parallel) and Fig. 4k was taken at perpendicular polarization, which minimizes the intensity. The array edge indicated by a red arrow in the DF image (Fig. 4i) is seen as a bright line only in the parallel arrangement of filters, which is what one can expect from the simulation.

The depolarization at wavelengths near resonance could be caused by different arguments of complex polarizability α along different ellipsoid axes as discussed for Ag nanoparticles in colloidal solution [36]. Indeed, phase differences between incident and scattered light from individual nanoparticles have been observed using a near-field

optical microscope [37]. However, this effect alone cannot explain the depolarization of S-polarized radiation since all orientations in the x,y plane for disk-shaped particles are equal. Hence, the depolarization is caused by collective interactions of particles in disordered arrays, where regions with localized resonant modes with different frequencies are formed. In comparison to strongly anisotropic nanoparticles [38], the depolarization would persist even for dense arrays of spheres. In order to characterize sample integrated depolarization, we calculate the ratio $w = C_{sca}(\mathbf{P}_+)/C_{sca}(\mathbf{P}_{||})$, namely, Eq. 5 computed for $\mathbf{P}$ components either x or y perpendicular to the electric field of incident radiation $\mathbf{E}_0$. The sample integrated depolarization ratio dependence on wavelength (Fig. 5) resembles the scattering spectra, and for P-polarized incidence, the maximum value of w (4 % for sample c) is approximately three times larger in comparison to S-polarized excitation. As can be seen in Fig. 4, local zones with extremely high depolarization (hot spots) are formed in a relatively broad spectral band near the scattering maximum. We also note that for P-polarized incidence, there are weak, but nonzero $\mathbf{P}$, components in the z direction, which indicates that particle anisotropy may cause additional depolarization even though the short axis plasmon resonance is relatively far in the ultraviolet spectral region.

In the remaining part of this section, we analyze various aspects of simulated arrays with parameters equal to sample (c) since the interesting properties are most prominent for this case.

Fig. 7 Calculated scattering spectra for array (c) illuminated at different angles and polarizations
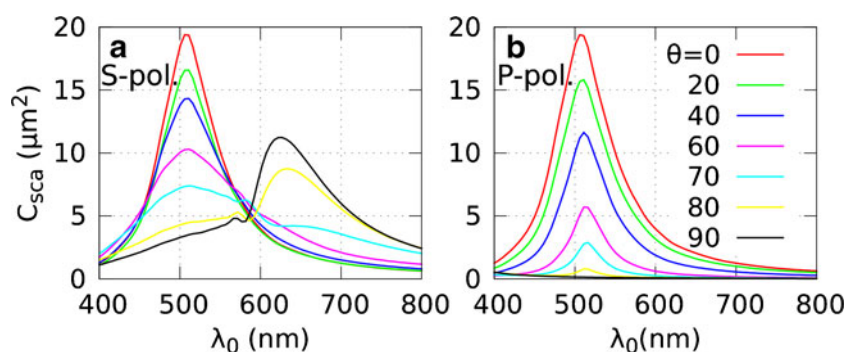
Intuitively, one can expect that for large arrays, the optical properties will become invariant to array size. The obvious question is how many dipoles are needed for numerical simulations to model the spectral response of the system. We analyze this in Fig. 6. Here, scattering efficiency Q_{sca} is obtained by division of C_{sca} with the number of particles and geometrical particle cross section. Spectra are shown in the same color for identical conditions except the azimuth angle $\phi = 0°$ and $\phi = 90°$, which is equivalent to sample rotation about the z axis. For small number of particles ($N = 10$), the spectra are relatively narrow and sensitive to sample rotation. This is what one can expect considering the orientation-dependent scattering of the simplest array, namely, particle pair [28, 32] and extending it to more complex asymmetric systems. For S-polarized incidence (Fig. 6a), one can identify two peaks, one centered around 510 nm and the second shifting to longer wavelength and gradually disappearing as the number of particles increases $N = 100, 200, 500$. The first peak can be attributed to the inner particles of the array, since its magnitude scales linearly with N, while the second peak belongs to the array edge and tends to disappear (increases less slowly) for increasing array size, since circumference scales as $N^{1/2}$. A further analysis is required to determine whether the red-shift of the second peak is due to variation of edge curvature or geometric resonance (standing waves) of collective dipole oscillations and reflection from array discontinuities. For P-polarized excitation (Fig. 6a), we observe slight broadening with no noticeable peak wavelength shifts. However, for both polarizations already at $N = 200$, the spectra become invariant to change of ϕ; hence, asymmetry in the array inner structure looses importance and the system acts like a continuous medium. Notably, there is little difference between calculated curves in cases $N = 1,000$ and $N = 2,200$. Therefore, $N = 2,000$ used to simulate the spectra is sufficiently large. However, the model for present set of parameters (c) overestimates the value of C_{sca} (Fig. 7), which exceeds the array area $S_{2,000}$ by a factor of 1.5, and from Fig. 6, it appears that the maximum scattering efficiency is constant for large values of N.

Finally, we show how scattering spectra change by variation of the incidence angle θ which we cannot verify experimentally, but can provide further insight into scattering properties of the studied arrays. As expected, for small values of θ and in particular for normal incidence, there is little difference between S- and P-polarized excitation (Fig. 7a, b). There is a significant broadening for S-polarized incidence with increasing value of θ, while for P-polarized incidence, the scattering reduces without change of width. P-polarized radiation does however excite plasmonic resonance along the short axis of the ellipsoids, in the ultraviolet part of the spectrum not shown in the graphs here. Only at very large values of θ (incidence nearly parallel to sample surface), a strongly red-shifted peak appears for S-polarized excitation, which indicates a different mode of collective array response. Comparison of Figs. 6a and 7a suggests that in both cases, the particles near array edge are responsible for the red-shifted peak.

Conclusions

We have analyzed experimentally and numerically various aspects of optical scattering by dense disordered Ag nanoparticle arrays and explained contrast formation in far-field scattering images. Tendencies obtained by CD model simulation are in qualitative agreement with experimental observations. From spectroscopic measurements, these arrays act as a continuum metamaterial with different properties in bulk (inner particles) and near edges (outer particles). Unlike periodic systems, these arrays produce relatively broad resonances, which may be of interest for photovoltaic applications. The method of fabrication and possibility to tune particle sizes may provide a viable way for production of multilayer devices [39]. Further tuning of ellipsoid shapes and optical resonances can be achieved by angled sputtering through the AAO membrane.

The important observation is the depolarized grain structure in scattered images at wavelengths near scattering resonance. We attribute these to collective interactions of particles in disordered arrays, where regions with localized resonant modes with different frequencies are formed. Upon excitation with coherent source, the apparently random interference patterns change rapidly with small variations of experimental conditions; thus, image analysis algorithms can be developed for sensing applications. The depolarization effect would persist even for disordered arrays of perfect spheres in Rayleigh limit. However, the presented numerical model underestimates the depolarization ratio of actual samples by excluding size distribution, particle anisotropy, and coupling to higher-order (quadrupolar) modes in larger particles.

Although silver was used in the presented study, the process of sample fabrication and numerical analysis can be generalized to other plasmonic nanoparticles, e.g., gold, where resonances of comparable structures can be observed in the red spectral region.

References

1. Daniel MC, Astruc D (2004) Chem Rev 104(1):293. doi:10.1021/cr030698+
2. Anker JN, Hall WP, Lyandres O, Shah NC, Zhao J, Van Duyne RP (2008) Nature Mater 7(6):442. doi:10.1038/nmat2162

3. Stiles PL, Dieringer JA, Shah NC, Van Duyne RP (2008) Annu Rev Anal Chem 1:601. doi:10.1146/annurev.anchem.1.031207.112814

4. Atwater HA, Polman A (2010) Nature Mater 9(3):205. doi:10.1038/nmat2629

5. Knight MW, Sobhani H, Nordlander P, Halas NJ (2011) Science 332(6030):702. doi:10.1126/science.1203056

6. Lal S, Link S, Halas NJ (2007) Nature Photon 1(11):641. doi:10.1038/nphoton.2007.223

7. Dirix Y, Bastiaansen C, Caseri W, Smith P (1999) Adv Mater 11(3):223. doi:10.1002/(SICI)1521-4095(199903)11:3<223::AID-ADMA223>3.0.CO;2-J

8. Genov DA, Sarychev AK, Shalaev VM, Wei A (2004) Nano Lett 4(1):153. doi:10.1021/nl0343710

9. McMillan BG, Berlouis LEA, Cruickshank FR, Pugh D, Brevet PF (2005) Appl Phys Lett 86(21):211912. doi:10.1063/1.1939070

10. Zou S, Schatz GC (2004) J Chem Phys 121(24):12606. doi:10.1063/1.1826036

11. Chu Y, Schonbrun E, Yang T, Crozier KB (2008) Appl Phys Lett 93(18):181108. doi:10.1063/1.3012365

12. Sung J, Hicks E, VanDuyne R, Spears K (2008) J Phys Chem C 112(11):4091. doi:10.1021/jp077332b

13. Zhao L, Kelly KL, Schatz GC (2003) J Phys Chem B 107(30):7343. doi:10.1021/jp034235j

14. Auguié B, Barnes WL (2009) Opt Lett 34(4):401. doi:10.1364/OL.34.000401

15. Nishijima Y, Rosa L, Juodkazis S (2012) Opt Express 20(10):11466. doi:10.1364/OE.20.011466

16. Grabar KC, Freeman RG, Hommer MB, Natan MJ (1995) Anal Chem 67(4):735. doi:10.1021/ac00100a008

17. Hanarp P, Käll M, Sutherland DS (2003) J Phys Chem B 107(24):5768. doi:10.1021/jp027562k

18. Haynes CL, Van Duyne RP (2001) J Phys Chem B 105(24):5599. doi:10.1021/jp010657m

19. Kim J, Kim J, Song KIB, Lee SQ, Kim EUNK, Choi SEUL, Lee Y, Park KHO (2003) J Microsc 209(3):236. doi:10.1046/j.1365-2818.2003.01132.x

20. Buzzi S, Galli M, Agio M, Löffler JF (2009) Appl Phys Lett 94(22):223115. doi:10.1063/1.3142426

21. Masuda H, Satoh M (1996) Jpn J Appl Phys 35(Part 2, No. 1B):L126. doi:10.1143/JJAP.35.L126

22. Wang HH, Liu CY, Wu SB, Liu NW, Peng CY, Chan TH, Hsu CF, Wang JK, Wang YL (2006) Adv Mater 18(4):491. doi:10.1002/adma.200501875

23. Nakayama K, Tanabe K, Atwater HA (2008) Appl Phys Lett 93(12):121904. doi:10.1063/1.2988288

24. Li AP, Müller F, Birner A, Nielsch K, Gösele U (1998) J Appl Phys 84(11):6023. doi:10.1063/1.368911

25. Schwind M, Miljković VD, Zäch M, Gusak V, Käll M, Zorić I, Johansson P (2012) ACS nano 6(11):9455. doi:10.1021/nn3021184

26. Pastore I, Poplausks R, Apsite I, Pastare I, Lombardi F, Erts D (2011) IOP Conf Ser Mater Sci Eng 23(1):012025. doi:10.1088/1757-899X/23/1/012025

27. Draine BT, Flatau PJ (1994) J Opt Soc Am A 11(4):1491. doi:10.1364/JOSAA.11.001491

28. Gunnarsson L, Rindzevicius T, Prikulis J, Kasemo B, Käll M, Zou S, Schatz GC (2005) J Phys Chem B 109(3):1079. doi:10.1021/jp049084e

29. Kuwata H, Tamaru H, Esumi K, Miyano K (2003) Appl Phys Lett 83(22):4625. doi:10.1063/1.1630351

30. Bohren CF, Huffman DR (1998) Absorption and scattering of light by small particles. Wiley VCH

31. Johnson PB, Christy RW (1972) Phys Rev B 6(12):4370. doi:10.1103/PhysRevB.6.4370

32. Rechberger W, Hohenau A, Leitner A, Krenn J, Lamprecht B, Aussenegg F (2003) Opt Comm 220(1-3):137. doi:10.1016/S0030-4018(03)01357-9

33. Anderson E, Bai Z, Bischof C, Blackford S, Demmel J, Dongarra J, Du Croz J, Greenbaum A, Hammarling S, McKenney A, Sorensen D (1999) LAPACK users' guide, 3rd edn. Society for Industrial and Applied Mathematics, Philadelphia

34. Draine BT (1988) Astrophys J 333:848. doi:10.1086/166795

35. Born M, Wolf E (1999) Principles of optics: electromagnetic theory of propagation, interference and diffraction of light. Cambridge University Press, Cambridge

36. Calander N, Gryczynski I, Gryczynski Z (2007) Chem Phys Lett 434(4–6):326. doi:10.1016/j.cplett.2006.12.003

37. Prikulis J, Xu H, Gunnarsson L, Käll M, Olin H (2002) J Appl Phys 92(10):6211. doi:10.1063/1.1516249

38. Khlebtsov BN, Khanadeev VA, Khlebtsov NG (2008) J Phys Chem C 112(33):12760. doi:10.1021/jp802874x

39. Pillai S, Green M (2010) Sol Energ Mat Sol Cells 94(9):1481. doi:10.1016/j.solmat.2010.02.046